

Geometrical Performance of Self-Phoretic Colloids and Microswimmers

Amir Nourhani^{1,2,*} and Paul E. Lammert^{1,2,†}

¹Center for Nanoscale Science, Pennsylvania State University, University Park, Pennsylvania 16802, USA

²Department of Physics, Pennsylvania State University, University Park, Pennsylvania 16802, USA

(Received 5 November 2015; revised manuscript received 1 April 2016; published 27 April 2016)

Within a unified formulation—encompassing self-electrophoresis, self-diffusiophoresis, and self-thermophoresis—we provide a simple integral kernel transforming the relevant surface flux to particle velocity for any spheroid with axisymmetric surface activity and uniform phoretic mobility. Appropriate scaling of the speed allows a dimensionless measure of the motion-producing performance of the motor shape and activity distribution across the surface. For bipartite designs with piecewise uniform flux over complementary surface regions, the performance is mapped out over the entire range of geometry (from discotic through spherical to rodlike shapes) and of bipartitioning, and intermediate aspect ratios that maximize performance are identified. Comparisons are made to experimental data from the literature.

DOI: 10.1103/PhysRevLett.116.178302

The challenge of powering motion at the (sub)microscale has motivated the development, over the past decade, of a variety of abiotic micromotors as building blocks of micromachines [1–4]. Artificial self-phoretic colloids, harvesting energy from the environment and transducing it to motion via active surfaces, offer a unique solution to this challenge [5–11]. The performance of a self-phoretic particle is determined by its shape and distribution of surface activity, whether the operative mechanism is self-diffusiophoresis [5], self-electrophoresis [7–9,12,13], or self-thermophoresis [14,15]. While quantitative analysis of these factors is essential for designing fast and efficient motors, studies have been mainly limited to spheres [16] or long thin rods; intermediate shapes and disks have been neglected (though sphere dimers [17] have also received attention).

In this Letter we seek to elucidate the determination of self-phoretic particle performance by both overall shape and surface distribution of activity, under common approximations of uniform phoretic mobility, thin interaction layer, and linearity. The practical benefit is a rational approach to higher performance—i.e., greater speed for the same energy (fuel) consumption. This is complementary to studying a genuine efficiency such as hydrodynamic dissipation divided by reaction enthalpy [16]. Within an approach unifying various self-phoresis mechanisms, we explore the design space of axisymmetric surface activity for the entire spheroid family, which smoothly interpolates from disks through spheres to needlelike shapes. The fundamental innovation on which the treatment turns is a simple integral kernel [Eqs. (2), (3) and Fig. 2] quantifying the *local* effectiveness of surface activity at producing motion. Applying this kernel to bipartite flux distributions, the performance of the full range of aspect ratio and bipartitioning (i.e., η_0 in Fig. 1) is mapped out in detail, and intermediate optimum geometries are identified.

Previously obscure trends, such as a nonmonotonic dependence of performance (scaled velocity) on the aspect ratio are thereby clarified. Explicit, closed-form expressions for the speed and performance are given for these designs in the Supplemental Material [18].

In Anderson’s unifying picture [19] for *passive* particles, phoresis is mediated by an externally imposed gradient of a field γ , such as concentration of a chemical species (diffusiophoresis), electric potential (electrophoresis), or temperature (thermophoresis). To leading order in interaction-layer thickness (assumed to be small compared to particle size), the tangential gradient of γ generates a slip velocity $v_{\text{slip}} = \mu_{\text{ph}} \nabla_s \gamma$ at the outer edge of the boundary layer. The phoretic mobility μ_{ph} usually depends quadratically on the interaction layer’s length scale [5,7,8,12]. In the case of a spheroidal particle, the resulting phoretic velocity is known [20] to be

$$\mathcal{U} = -\frac{1}{3\mathcal{V}} \int_S \mu_{\text{ph}}(\hat{n} \cdot \mathbf{r}) \nabla_s \gamma dS, \quad (1)$$

where \hat{n} is the outward-pointing unit vector normal to the surface, \mathbf{r} is position relative to the spheroid center, and \mathcal{V} is

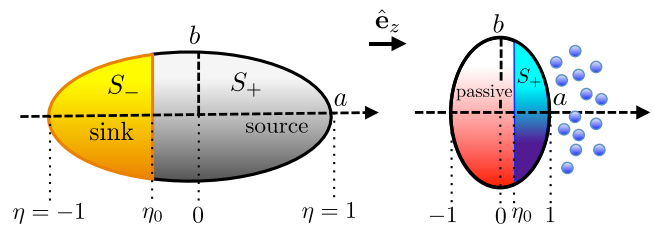


FIG. 1. Standard bipartite geometry on the spheroid. The border between the two regions corresponds to the scaled z coordinate $\eta = \eta_0$. (η is equivalent to $\cos \theta$ for a sphere.) In the source-sink case, both sides on the surface are active (left panel), while in the source-inert case only one side is active (right panel).

particle volume. We approximate μ_{ph} to be uniform, as is commonly done [5,7,8,12].

In phoresis of passive particles, γ is controlled externally; however, a self-phoretic particle sustains the gradient of γ itself by generating a heterogeneous surface flux Γ . Therefore, it may be more useful and perspicuous to relate the particle velocity directly to the pattern of surface activity Γ , rather than indirectly through γ [5–11]. The motion of present-day motors has little effect on chemical kinetics at their surfaces; only the resulting flux is needed for our study [7]. This is because the diffusion of an ion or molecule with $D \sim 10^{-9}$ m²/s over the length of a 1- μ m motor corresponds to an effective speed of 1 mm/s, much larger than the speed of the particle. To leading order in interaction layer thickness and flux, γ satisfies the Laplace equation with boundary condition $\Gamma = -\mathcal{D}\hat{n} \cdot \nabla\gamma$, where \mathcal{D} involves a diffusion coefficient or conductivity. Then γ is given, up to a constant, as $\mathcal{D}^{-1}\mathcal{L}\{\Gamma\}$ [7], where \mathcal{L} is a geometry-dependent Neumann-to-Dirichlet operator. Thus, in the limit of small Péclet number, self-phoretic velocity of a spheroid is $\mathbf{U} = -(\mu_{\text{ph}}/3\mathcal{V}\mathcal{D}) \int_S \hat{n} \cdot \mathbf{r} \nabla_s \mathcal{L}\{\Gamma\} dS$. For axisymmetric flux Γ , a remarkable simplification [18] allows the explicit expression

$$\mathbf{U} = U\hat{\mathbf{e}}_z = \hat{\mathbf{e}}_z \frac{(-\mu_{\text{ph}})}{2\mathcal{D}} \int_{-1}^1 K(\eta; a/b) \Gamma(\eta) d\eta, \quad (2)$$

where, as depicted in Fig. 1, $\hat{\mathbf{e}}_z$ is the symmetry direction, a (b) is the half-length along (perpendicular to) the symmetry axis, and $-1 \leq \eta \equiv z/a \leq 1$. The dimensionless kernel

$$K(\eta; a/b) = \frac{\eta}{\sqrt{\eta^2 + (a/b)^2(1 - \eta^2)}}, \quad (3)$$

expressing the contribution of flux at each location on the motor surface to motion, is the main protagonist of this Letter.

Inspection of the graphs of $K(\eta; a/b)$, shown in Fig. 2 for a range of aspect ratios a/b , is already quite revealing. $K(\eta; \ell^{-1})$ is the reflection of $K(\eta; \ell)$ across the diagonal $\ell \equiv a/b = 1$. Thus, for a sphere ($a/b = 1$), K degenerates to a straight line, a known result [9]. Deviation from sphericity by the increase of the aspect ratio a/b increasingly suppresses $|K|$ around the equator $\eta = 0$. The earliest generation of self-electrophoretic cylindrical rods [3] had an aspect ratio of about 5, so this effect is strong even under ordinary conditions. One message is clear: for a thin rodlike particle, only surface activity near the poles contributes significantly to self-phoresis. Thus, in designing a motor with a large aspect ratio, details of the surface activity around the equatorial region are insignificant and may be chosen for convenience. This phenomenon explains why, in numerical simulation of self-electrophoretic long rods, a jump discontinuity in surface cation flux distribution

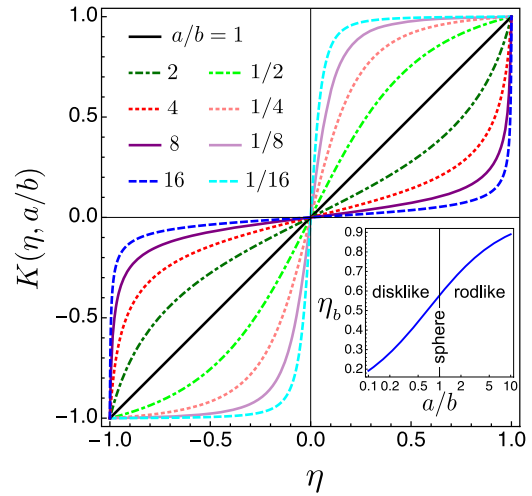


FIG. 2. The spheroid velocity kernel, Eq. (3), for a range of aspect ratios. $K(\eta; \ell^{-1})$ is just $K(\eta; \ell)$ reflected across the diagonal $\ell \equiv a/b = 1$. For a sphere ($a/b = 1$) the kernel is simply linear. On the prolate side ($a/b > 1$), a zone of suppressed effectiveness moves outward from the equator with an increasing aspect ratio, and on the oblate side ($a/b < 1$) a zone of enhanced effectiveness moves inward from the poles as the aspect ratio is decreased. Inset: The “belly” η_b is the point at which $dK/d\eta = 1$, and it provides a quantitative expression of the division into effective and ineffective regions. The plot shows η_b as a function of the aspect ratio.

around the equator can provide the essential physics and give consistent results with experimental observations [21].

In contrast, as the particle deviates from sphericity toward a discoidal shape, zones of large $|K|$ expand from the poles toward the equator. This suggests, perhaps rather surprisingly, that oblate designs can be much more effective at converting chemical activity into speed. This is a region of the design space which deserves more experimental attention than it has received to date.

Now, we exploit the kernel (3) to explore specific parametrized families of motor designs. Since simple models without too many parameters are best for revealing generic trends, we consider bipartite models with flux taking distinct uniform values over two complementary regions of the surface. There are two families to be considered. Source-inert (or sink-inert) particles occur in cases of self-diffusiophoresis and self-thermophoresis, with an active region which is a pure source (or sink), and a passive region. Self-electrophoretic particles, by contrast, have a source-sink configuration. Since the net ion flux from the entire surface must be zero, equal quantities of active ions are produced on the source region and consumed on the sink.

The idea now is to isolate from the raw speed (2) a performance characteristic capturing the contribution of geometry alone—meaning the shape of the particle and the relative distribution of activity Γ over the particle surface. A natural speed scale independent of these elements is

$$U^* = -\frac{\mu_{\text{ph}} \|\Gamma\|}{2D S}, \quad (4)$$

with $\|\Gamma\| = \int_S |\Gamma| dA$ and S the total surface area. Thus, we consider the dimensionless scaled velocity

$$\frac{U}{U^*} = \frac{S}{\|\Gamma\|} \int_{-1}^1 K(\eta; \ell) \Gamma(\eta) d\eta \quad (5)$$

as a measure of geometrical performance; hence, we sometimes call it “performance.” This quantity is well defined only for active particles ($U^* \neq 0$). If S is regarded as fixed, even as the shape and activity distribution are varied, U/U^* is proportional to speed produced per unit total activity, and is a sort of efficiency in that sense. Using U/U^* , we shall discuss the performance of source-since and source-inert configurations. Closed-form expressions are given in the Supplemental Material [18].

Source-sink design.—A source-sink design (see Fig. 1) has a uniform positive flux over the source region $\{\eta > \eta_0\}$ of area S_+ , and a balancing uniform negative flux over the sink region $\{\eta < -\eta_0\}$ of area $S_- = S - S_+$. Using the constraint of zero net flux in the definition (5), the scaled velocity for this family is

$$\text{source-sink : } \frac{U}{U^*} = \frac{S^2}{2S_- S_+} \int_{|\eta_0|}^1 K(\eta; \ell) d\eta, \quad (6)$$

which is even in η_0 , as required by symmetry. Plots of the scaled velocity for a variety of values of η_0 are depicted in Fig. 3 as a function of the aspect ratio. Since zero source area implies zero speed, it may seem a bit surprising that U/U^* does not tend to zero as $\eta_0 \rightarrow \pm 1$ at fixed a/b . But if $\eta_0 = \pm 1$, $U^* \neq 0$ is impossible, so we must require $|\eta_0| < 1$. An apt analogy is to a heat engine, the efficiency of which is increased by operating it more slowly. Yet efficiency is not maximized at zero speed of operation, for it is ill defined there. In the discoidal regime, speed *decreases* monotonically as $|\eta_0|$ is increased, whereas in the prolate regime, it *increases* monotonically. Note that this involves comparing particles of identical size and shape, so that the same trend is valid if total flux is held fixed. For $\eta_0 = 0$, the source-sink performance U/U^* tends to 2 as $a/b \rightarrow 0$. For small values of η_0 , oblate designs have highest performance. The relative advantage of discoidal designs decreases as η_0 increases. At $\eta_0 \approx 0.655$, the maximum performance is for a sphere; beyond that, it lies in the prolate range. As a result, when $\eta_0 \gtrsim 0.655$, for each oblate shape ($a/b < 1$) there is a prolate shape with the same scaled velocity. It has been previously noted [9] that the scaled speed of a sphere is insensitive to η_0 . Now we see that this feature is specific to the sphere. The phenomenon of the peak of U/U^* moving up and to the right as η_0 is increased beyond 0.655 is quantified in the inset of Fig. 3. The dashed red curve shows the maximum value $[U/U^*]_{\text{max}}$, and the blue solid

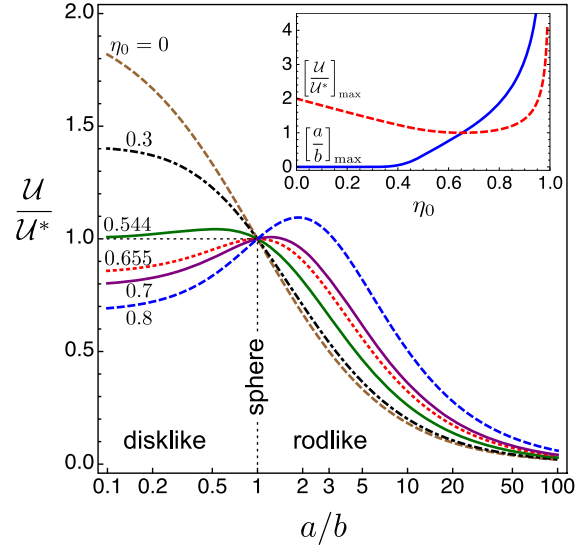


FIG. 3. Performance of a source-sink motor as a function of the aspect ratio for various values of the source-sink boundary η_0 . The limit as the aspect ratio tends to zero is $\lim_{a/b \rightarrow 0} U/U^* = 2(1 - |\eta_0|)/(1 - \eta_0^4)$. At $\eta_0 = 0$, the thin disk limit of the scaled velocity is thus 2, and it exceeds 1 (the spherical value) for $\eta_0 < 0.544$. At $\eta_0 = \sqrt{3/7} \approx 0.655$, the derivative at the spherical point is zero. Below this value, the maximum is for an oblate spheroid, and above it, for a prolate spheroid, as also shown in the inset. Inset: The dashed red curve shows the maximum attainable value of the scaled velocity over all aspect ratios for a given source-sink boundary η_0 . The solid blue curve shows the aspect ratio at which that maximum is attained. Note that the vertical scale therefore quantifies different things for the two curves. The maximizing aspect ratio $[a/b]_{\text{max}}$ ratio is very nearly zero for all $\eta_0 \lesssim 0.35$.

curve, the aspect ratio $[a/b]_{\text{max}}$ at which it occurs. Only non-negative η_0 are shown since U/U^* is even in η_0 . Over most of the range of η_0 , the variation is no more than a factor of 2. As $\eta_0 \rightarrow 1$, $[U/U^*]_{\text{max}}$ diverges, but reaching it requires a/b to diverge. Realistically, neglected effects and scales, such as the interaction-layer thickness, will cut off the divergence.

For the common antisymmetric design $\eta_0 = 0$, Eq. (6) yields the simple explicit expression $U = 2(-\mu_{\text{ph}}\alpha/2D)/(1 + a/b)$, with α the uniform value of Γ on the source. Dhar *et al.* [22] measured speeds of cylindrical half-Au, half-Pt rods of the same radius but differing diameters in the same medium. Approximating those shapes by spheroids and applying the source-sink model with the same value of α for all rods leaves a single fitting parameter. The fit in Fig. 4 seems good enough that if data were available for a variety of fuel concentrations, it might be possible to discover useful information about the reaction kinetics.

The simple formula in the previous paragraph is exact for all spheroids. Some expressions for the slender body limit $a/b \gg 1$ that have appeared in the literature [3,5,6] contain logarithmic factors; these can now be seen to be spurious,

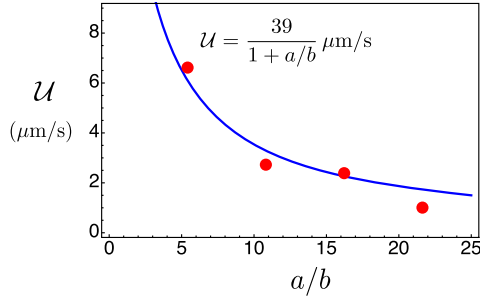


FIG. 4. Fit of speed measurements [22] on half-Au, half-Pt cylinders of varying length to the formula $U = 2(-\mu_{\text{ph}}\alpha/2D)/(1 + a/b)$ derived for $\eta_0 = 0$ spheroids. The single fitting parameter is $-\mu_{\text{ph}}\alpha/2D \approx 19.5 \mu\text{m/s}$, which is the velocity scale characterizing these motors.

the correct asymptotic behavior being simply b/a . This has also been noted in [11].

Source-inert or sink-inert designs.—The difference between a pure source and a pure sink configuration is a simple matter of sign, so we consider just the source case, with uniform source over the region $\{\eta > \eta_0\}$ of area S_+ ; the rest of the motor surface is inert (Fig. 1). Equation (5) yields

$$\text{source-inert: } \frac{U}{U^*} = \frac{S}{S_+} \int_{|\eta_0|}^1 K(\eta; \ell) d\eta. \quad (7)$$

We concentrate now on differences from the source-sink geometry. In contrast to that case, U/U^* is not even in η_0 . One aspect of this difference is that, at a fixed aspect ratio, U/U^* is bounded away from zero as $\eta_0 \rightarrow 1$, similar to source-sink scenario, but tends to zero as $\eta_0 \rightarrow -1$, because nonzero U^* makes sense at $\eta_0 = -1$. Correspondingly, the proper domain is $-1 \leq \eta_0 < 1$. Figure 5 shows a range for both small source ($\eta_0 > 0$) and large source ($\eta_0 < 0$). For $\eta_0 > 0$, the curves are qualitatively similar to those for a source-sink particle. For $\eta_0 < 0$, however, the two cases differ greatly. In particular, the performance is a monotonically decreasing function of the aspect ratio for all $\eta_0 \leq 0$. In the spherical case ($a/b = 1$), the performance $U/U^* = 1 + \eta_0$ is not independent of η_0 , as it was for a source-sink particle, but decreases with an increase in the source area. In the extreme discotic limit $a \ll b$, $U/U^* = 2(1 - |\eta_0|)/(1 - \eta_0|\eta_0|)$ has a maximum value of 2 at the half-and-half geometry $\eta_0 = 0$, as for a source-sink particle, and decreases as $|\eta_0|$ increases. The maximum attainable scaled velocity at fixed η_0 and the corresponding value of the aspect ratio at which it is attained are also qualitatively similar to the source-sink case for $\eta_0 > 0$. However, as η_0 decreases from zero to -1 , the maximum is attained only in the limit $a/b \rightarrow 0$; $[U/U^*]_{\text{max}}$ drops monotonically from 2 to zero; as η_0 becomes more negative, the source is spread more evenly across the surface so that activity at one end counteracts that at the other. At constant $\|\Gamma\|/S_+$,

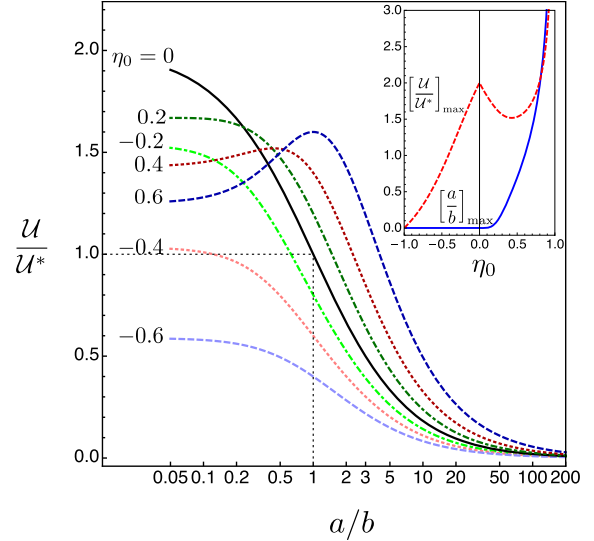


FIG. 5. Performance of a pure-source motor as a function of the aspect ratio for various values of the source-inert boundary η_0 . Inset: Maximum attainable scaled velocity at fixed η_0 (dashed red), and the aspect ratio at which it is attained (solid blue). Compare to Fig. 3 for the source-sink case.

regardless of the value of η_0 , the (nonscaled) speed is always maximum for extreme oblate particles [23], as previously observed for $\eta_0 = 0$ [5].

Understanding the effect of geometry and surface activity on autonomous active colloids is essential for designing powered machines with tuned properties at nano- and microscale. While in phoresis of passive particles the driving field is external; active colloids harvest energy from their environment and self-generate the driving field through a surface flux. The self-phoretic velocity expression (2), connecting the motor velocity to its shape and distribution of surface flux, is general across the various self-phoretic mechanisms, opening the route to a unified formulation connecting velocity to surface activity and flux for various geometries with uniform phoretic mobility. For an arbitrary axisymmetric geometry with axisymmetric flux, in consequence of the linearity and scaling properties of the governing equations, a formula like Eq. (2) holds with some kernel K expressing the contribution of flux at each location on the motor surface to motion. The spheroid family distinguishes itself through the explicit flux-to-speed kernel (3). Since phoretic mobility μ_{ph} and diffusivity D are constant material properties, dimensional analysis then shows that K is dimensionless. Therefore, provided $\Gamma(\eta)$ is held constant, the size of the particle drops out. For a given self-phoresis mechanism, $\Gamma(\eta)$ may have an implicit size dependence when directly controllable conditions such as fuel concentration are maintained constant [7]. However, such dependences vary from one self-phoretic mechanism to another, and thus fall outside our unifying scope. For unifying studies across different

self-phoretic mechanisms, we regard $\Gamma(\eta)$ as simply given in expression (2).

Even with simple assumptions regarding the surface flux distribution, the theory makes good contact with experimental results, as Fig. 4 shows, and explains the consistency of experimental observation with numerical simulation results for a discontinuous flux jump around the equator in Ref. [21]. Oblate (discotic) spheroids—which have, to our knowledge, received no previous experimental attention—emerge from this survey of the design space as potentially interesting candidates for experimental investigation.

The authors are grateful to Professor Vincent H. Crespi, Professor Wei Wang, and Dr. Cristiano Nisoli for their insightful comments and suggestions. This work was funded by the Penn State Materials Research Science and Engineering Center, Center for Nanoscale Science, under the National Science Foundation Award No. DMR-1420620.

*nourhani@psu.edu

†lammert@psu.edu

- [1] S. J. Ebbens and J. R. Howse, *Soft Matter* **6**, 726 (2010).
- [2] J. Wang, *Nanomachines: Fundamentals and Applications* (Wiley-VCH, Weinheim, Germany 2013).
- [3] W. Paxton, K. Kistler, C. Olmeda, A. Sen, S. S. Angelo, Y. Cao, T. Mallouk, P. Lammert, and V. Crespi, *J. Am. Chem. Soc.* **126**, 13424 (2004).
- [4] J. G. Gibbs and P. Fischer, *Chem. Commun. (Cambridge)* **51**, 4192 (2015).
- [5] M. N. Popescu, S. Dietrich, M. Tasinkevych, and J. Ralston, *Eur. Phys. J. E* **31**, 351 (2010).
- [6] R. Golestanian, T. B. Liverpool, and A. Ajdari, *New J. Phys.* **9**, 126 (2007).
- [7] A. Nourhani, V. H. Crespi, and P. E. Lammert, *Phys. Rev. E* **91**, 062303 (2015).
- [8] A. Nourhani, V. H. Crespi, P. E. Lammert, and A. Borhan, *Phys. Fluids* **27**, 092002 (2015).
- [9] A. Nourhani, P. E. Lammert, V. H. Crespi, and A. Borhan, *Phys. Fluids* **27**, 012001 (2015).
- [10] S. Ebbens, M.-H. Tu, J. R. Howse, and R. Golestanian, *Phys. Rev. E* **85**, 020401(R) (2012).
- [11] O. Schnitzer and E. Yariv, *Phys. Fluids* **27**, 031701 (2015).
- [12] E. Yariv, *Proc. R. Soc. A* **467**, 1645 (2011).
- [13] B. Sabass and U. Seifert, *J. Chem. Phys.* **136**, 214507 (2012).
- [14] H. R. Jiang, N. Yoshinaga, and M. Sano, *Phys. Rev. Lett.* **105**, 268302 (2010).
- [15] R. Golestanian, *Phys. Rev. Lett.* **108**, 038303 (2012).
- [16] P. Kreissl, C. Holm, and J. de Graaf, [arXiv:1602.07883](https://arxiv.org/abs/1602.07883).
- [17] S. Y. Reigh and R. Kapral, *Soft Matter* **11**, 3149 (2015).
- [18] See Supplemental Material at <http://link.aps.org/supplemental/10.1103/PhysRevLett.116.178302> for details of the derivation.
- [19] J. L. Anderson, *Annu. Rev. Fluid Mech.* **21**, 61 (1989).
- [20] M. C. Fair and J. L. Anderson, *J. Colloid Interface Sci.* **127**, 388 (1989).
- [21] W. Wang, T.-Y. Chiang, D. Velegol, and T. E. Mallouk, *J. Am. Chem. Soc.* **135**, 10557 (2013).
- [22] P. Dhar, T. M. Fischer, Y. Wang, T. E. Mallouk, W. F. Paxton, and A. Sen, *Nano Lett.* **6**, 66 (2006).
- [23] See Supplemental Material at <http://link.aps.org/supplemental/10.1103/PhysRevLett.116.178302>, Sec. III.

Supplementary Information for “Geometrical performance of self-phoretic colloids and microswimmers”

Amir Nourhani and Paul E. Lammert

*Center for Nanoscale Science, The Pennsylvania State University, University Park, PA 16802 and
Department of Physics, The Pennsylvania State University, University Park, PA 16802*

Section 1 provides the derivation of the fundamental integral kernel $K(\eta; \ell)$. Section 2 provides the closed form expressions needed to evaluate velocities, scaled or unscaled, of bipartite source/sink and source/inert particles, as well as limits for $\eta_0 \rightarrow 0$. Section 3 gives supplementary results for the velocity of the diffusiophoretic model of Popescu *et al.* [5]

1. DERIVATION OF KERNEL

Here, we obtain the integration kernel $K(\eta, a/b)$ for Eq. (1) in the manuscript,

$$\mathbf{u} = \hat{\mathbf{e}}_z \frac{(-\mu_{ph})}{2\mathcal{D}} \int_{-1}^1 K(\eta, a/b) \Gamma(\eta) d\eta. \quad (\text{S1})$$

Adjacent to the motor surface the fluid is subjected to a slip velocity $\mathbf{v}_{\text{slip}} = \mu_{ph} \nabla_s \gamma$ where γ is harmonic ($\nabla^2 \gamma = 0$) with far-field constant value γ_∞ . The particle is a spheroid of semi-major axis a and semi-minor axis b with volume $\mathcal{V} = \frac{4}{3}\pi b^2 a$. According to the self-consistent nonlocal feedback (SCNLF) theory [7], the field γ can be obtained from the axisymmetric flux Γ using a geometry-dependent Neumann-to-Dirichlet operator \mathcal{L} . That is,

$$\Gamma = -\mathcal{D} \hat{\mathbf{n}} \cdot \nabla \gamma \quad \rightsquigarrow \quad (\mathcal{D}^{-1} \Gamma) = -\hat{\mathbf{n}} \cdot \nabla \gamma \quad \rightsquigarrow \quad \gamma = \gamma_\infty + \mathcal{L}\{\mathcal{D}^{-1} \Gamma\}. \quad (\text{S2})$$

Since the geometry and flux Γ are axisymmetric, the self-phoretic particle moves along its symmetry axis $\hat{\mathbf{e}}_z$. We employ the prolate spheroidal coordinates with the metric factors

$$g_1(\xi, \eta) = \xi_s \sqrt{(\xi^2 - 1)/(\xi^2 - \eta^2)}, \quad g_2(\xi, \eta) = \xi_s \sqrt{(1 - \eta^2)/(\xi^2 - \eta^2)}, \quad (\text{S3})$$

which, on the spheroid's surface $\xi_s = \varepsilon^{-1}$, turn into

$$\varepsilon g_{1,s}(\eta) := \varepsilon g_1(\xi_s, \eta) = \frac{1}{a} \hat{\mathbf{n}} \cdot \mathbf{r} = \sqrt{\frac{1 - \varepsilon^2}{1 - \varepsilon^2 \eta^2}}, \quad g_2(\eta) := g_{2,s}(\xi_s, \eta) = \hat{\mathbf{e}}_\eta \cdot \hat{\mathbf{e}}_z = \sqrt{\frac{1 - \eta^2}{1 - \varepsilon^2 \eta^2}}. \quad (\text{S4})$$

We also need the surface gradient operator $\nabla_s = \hat{\mathbf{e}}_\eta a^{-1} g_{2,s}(\eta) \partial_\eta$, and the differential surface element $dS = 2\pi b^2 d\eta / (\varepsilon g_{1,s})$ on the spheroid. Then, using Fair and Anderson's integral expression [19] for particle velocity based on slip velocity we obtain

$$\begin{aligned} \mathbf{u} &= -\frac{1}{3\mathcal{V}} \int_S (\hat{\mathbf{n}} \cdot \mathbf{r}) \mathbf{v}_{\text{slip}} dS = -\hat{\mathbf{e}}_z \frac{\mu_{ph}}{4\pi b^2 a} \int_S (\hat{\mathbf{n}} \cdot \mathbf{r}) (\hat{\mathbf{e}}_z \cdot \nabla_s \mathcal{L}\{\mathcal{D}^{-1} \Gamma\}) dS \\ &= -\hat{\mathbf{e}}_z \frac{\mu_{ph}}{4\pi b^2 a} \int_{-1}^1 [a \varepsilon g_{1,s}(\eta)] [a^{-1} g_{2,s}^2(\eta) \partial_\eta (\mathcal{L}\{\mathcal{D}^{-1} \Gamma\})] \frac{2\pi b^2 d\eta}{\varepsilon g_{1,s}} = -\hat{\mathbf{e}}_z \frac{\mu_{ph}}{2a} \int_{-1}^1 g_{2,s}^2(\eta) \partial_\eta (\mathcal{L}\{\mathcal{D}^{-1} \Gamma\}) d\eta \end{aligned} \quad (\text{S5})$$

If we can write $g_{1,s} \partial_\eta g_2^2$ in terms of the normal gradient $g_{1,s} \partial_\xi$ of a harmonic field, we can use the fact that $\int_s dS \alpha \mathcal{L} \beta = \int_s dS \beta \mathcal{L} \alpha$ for any surface fields α, β in the domain of \mathcal{L} . So,

$$\begin{aligned} g_{1,s} \frac{\partial g_2^2}{\partial \eta} &= g_{1,s} \frac{1}{\varepsilon^2} \frac{\partial}{\partial \eta} \left(\frac{1 - \eta^2}{\xi^2 - \eta^2} \right) = g_{1,s} \frac{1}{\varepsilon^2} \frac{-2\eta(\xi^2 - 1)}{(\xi^2 - \eta^2)^2} = g_{1,s} \frac{\eta(\xi^2 - 1)}{\xi \varepsilon^2} \frac{-2\xi}{(\xi^2 - \eta^2)^2} = g_{1,s} \frac{\eta(\xi^2 - 1)}{\xi \varepsilon^2} \partial_\xi \left[\frac{1}{\xi^2 - \eta^2} \right] \\ &= g_{1,s} \frac{\eta(\xi^2 - 1)}{\xi \varepsilon^2} \frac{1}{2\eta} \partial_\xi \left[\frac{1}{\xi - \eta} - \frac{1}{\xi + \eta} \right] \stackrel{S}{=} g_{1,s} \frac{(\varepsilon^{-2} - 1)}{2\varepsilon} \partial_\xi \left[\frac{1}{\xi - \eta} - \frac{1}{\xi + \eta} \right] \\ &\stackrel{S}{=} g_{1,s} \frac{1 - \varepsilon^2}{2\varepsilon^3} \partial_\xi \left[\frac{1}{\xi - \eta} - \frac{1}{\xi + \eta} \right] \stackrel{S}{=} \frac{1 - \varepsilon^2}{2\varepsilon^3} a \hat{\mathbf{n}} \cdot \nabla \left[\frac{1}{\xi - \eta} - \frac{1}{\xi + \eta} \right] \end{aligned} \quad (\text{S6})$$

where ‘S’ above the equals sign means the equality holds only at the particle surface. Now, we need to show that $1/(\xi - \eta)$ and $1/(\xi + \eta)$ are harmonic; then the function in parentheses in the final expression of (S6) will be also. We just make a straightforward check. In spheroidal coordinates, the Laplacian acting on an axisymmetric field is

$$\nabla^2 = \frac{1}{\varepsilon^2(\xi^2 - \eta^2)} \left[\frac{\partial}{\partial \xi}(\xi^2 - 1) \frac{\partial}{\partial \xi} + \frac{\partial}{\partial \eta}(1 - \eta^2) \frac{\partial}{\partial \eta} \right]. \quad (\text{S7})$$

Hence, for differentiation with respect to η we have

$$\frac{\partial}{\partial \eta}(1 - \eta^2) \frac{\partial}{\partial \eta} \frac{1}{\xi - \eta} = \left[(1 - \eta^2) \frac{\partial^2}{\partial \eta^2} - 2\eta \frac{\partial}{\partial \eta} \right] \frac{1}{\xi - \eta} = \frac{2(1 - \eta^2)}{(\xi - \eta)^3} - \frac{2\eta}{(\xi - \eta)^2} = 2 \frac{1 - \eta\xi}{(\xi - \eta)^3}. \quad (\text{S8})$$

Note that if we swap ξ and η in this final expression, the sign is changed. On the other hand,

$$\frac{\partial}{\partial \xi}(\xi^2 - 1) \frac{\partial}{\partial \xi} \frac{1}{\xi - \eta} = \frac{\partial}{\partial \xi}(1 - \xi^2) \frac{\partial}{\partial \xi} \frac{1}{\eta - \xi}, \quad (\text{S9})$$

and this is exactly the left-hand side of (S8) with ξ and η swapped. Thus, this produces something that exactly cancels the term we already computed. And, therefore, $\nabla^2(\xi - \eta)^{-1} = 0$. Since reflection across the x - y plane is a symmetry of the Laplacian, it follows that $1/(\xi + \eta)$ and the function in parentheses in (S6) are harmonic as well.

Now, we can evaluate the integral in Eq. (S5) using $g_{2,s}(\pm 1) = 0$ and integrating by parts,

$$\begin{aligned} \int_{-1}^1 d\eta g_{2,s}^2 \partial_\eta (\mathcal{L}\{\mathcal{D}^{-1}\Gamma\}) &= g_{2,s}^2 \mathcal{L}\{\mathcal{D}^{-1}\Gamma\} \Big|_{-1}^1 - \int_{-1}^1 \frac{\partial g_{2,s}^2}{\partial \eta} \mathcal{L}\{\mathcal{D}^{-1}\Gamma\} d\eta = -\frac{\varepsilon}{2\pi b^2} \int_{-1}^1 g_{1,s} \frac{\partial g_{2,s}^2}{\partial \eta} \mathcal{L}\{\mathcal{D}^{-1}\Gamma\} dS \\ &= -\frac{\varepsilon}{2\pi b^2} \int_{-1}^1 (\mathcal{D}^{-1}\Gamma) \mathcal{L}\{g_{1,s} \partial_\eta g_{2,s}^2\} dS = -\int_{-1}^1 (\mathcal{D}^{-1}\Gamma) \frac{1}{g_{1,s}} \mathcal{L}\{g_{1,s} \partial_\eta g_{2,s}^2\} d\eta \\ &= -\frac{1 - \varepsilon^2}{2\varepsilon^3} \int_{-1}^1 (\mathcal{D}^{-1}\Gamma) \frac{1}{g_{1,s}} \mathcal{L}\left\{ a\hat{n} \cdot \nabla \left[\frac{1}{\xi - \eta} - \frac{1}{\xi + \eta} \right] \right\} d\eta \\ &= a \frac{1 - \varepsilon^2}{2\varepsilon^3} \int_{-1}^1 (\mathcal{D}^{-1}\Gamma) \frac{1}{g_{1,s}} \left[\frac{1}{\xi_s - \eta} - \frac{1}{\xi_s + \eta} \right] d\eta \\ &= a \int_{-1}^1 (\mathcal{D}^{-1}\Gamma) (\xi_s^2 - 1) \frac{\eta}{\xi_s^2 - \eta^2} \sqrt{\frac{\xi_s^2 - \eta^2}{\xi_s^2 - 1}} d\eta \\ &= a \int_{-1}^1 (\mathcal{D}^{-1}\Gamma) \eta \sqrt{\frac{\xi_s^2 - 1}{\xi_s^2 - \eta^2}} d\eta \end{aligned} \quad (\text{S10})$$

Also, defining $\ell = a/b$ we have

$$\frac{\xi^2 - 1}{\xi^2 - \eta^2} = \frac{1 - \varepsilon^2}{1 - \varepsilon^2 \eta^2} = \frac{1 - (1 - \ell^{-2})}{1 - (1 - \ell^{-2})\eta^2} = \frac{\ell^{-2}}{1 - (1 - \ell^{-2})\eta^2} = \frac{1}{\ell^2 - (\ell^2 - 1)\eta^2} = \frac{1}{\eta^2 + (1 - \eta^2)\ell^2} \quad (\text{S11})$$

Plugging Eqs. (S10) and (S11) into (S5) gives

$$\mathbf{u} = \hat{\mathbf{e}}_z \frac{(-\mu_{ph})}{2\mathcal{D}} \int_{-1}^1 \frac{\eta}{\sqrt{\eta^2 + \ell^2(1 - \eta^2)}} \Gamma d\eta \quad (\text{S12})$$

Therefore, we obtain the kernel [Eq. (2) of the manuscript],

$$K(\eta, a/b) = \eta[\eta^2 + (a/b)^2(1 - \eta^2)]^{-1/2} \quad (\text{S13})$$

2. CLOSED FORM EXPRESSIONS

A. Components

Noting that

$$K(\eta; \ell) = \frac{1}{1 - \ell^2} \frac{d}{d\eta} [\eta^2 + \ell^2(1 - \eta^2)]^{1/2}, \quad (\text{S14})$$

it immediately follows that

$$\int_{\eta_0}^1 K(\eta; \ell) d\eta = - \int_{-1}^{\eta_0} K(\eta; \ell) d\eta = \frac{1 - \sqrt{\eta_0^2 + \ell^2(1 - \eta_0^2)}}{1 - \ell^2}. \quad (\text{S15})$$

For evaluating velocities (as in Section 3), this suffices. For scaled velocities, surface areas are also needed. Denoting the surface area of the region $\{\eta_0 < \eta \leq 1\}$ by $S(\eta_0, 1)$, we have

$$2 \frac{S(\eta_0, 1)}{S} = 1 - \frac{\mathcal{A}(\ell, \eta_0)}{\mathcal{A}(\ell, 1)}, \quad (\text{S16})$$

with the auxiliary function \mathcal{A} given by

$$\mathcal{A}(\ell, \eta) = f\left(\eta\sqrt{1 - \ell^2}\right), \quad f(x) = x\sqrt{1 - x^2} + \sin^{-1} x. \quad (\text{S17})$$

B. Scaled Velocities

In the standard source/sink configuration, the flux is uniformly equal to $\alpha_+ > 0$ over the source region of area $S_+ = S(\eta_0, 1)$, and to $\alpha_- < 0$ over the sink region of area $S_- = S - S_+$. With total absolute flux $\|\Gamma\| := \int_S |\Gamma| dS = \alpha_+ S_+ - \alpha_- S_-$, the condition of zero net flux $\int_S \Gamma dS = 0 = \alpha_+ S_+ + \alpha_- S_- = 0$ yields $\alpha_{\pm} = \pm \|\Gamma\| / (2S_{\pm})$. Using Eqs. (S15) and (S16), we then find

$$\begin{aligned} \text{source/sink: } \frac{\mathcal{U}}{\mathcal{U}^*} &= \frac{S}{\|\Gamma\|} \int_{-1}^1 K(\eta; \ell) \Gamma(\eta) d\eta = \frac{S}{\|\Gamma\|} \left[-\frac{\|\Gamma\|}{2S_-} \int_{-1}^{\eta_0} K(\eta; \ell) d\eta + \frac{\|\Gamma\|}{2S_+} \int_{\eta_0}^1 K(\eta; \ell) d\eta \right] \\ &= S \left(\frac{1}{2S_-} + \frac{1}{2S_+} \right) \int_{\eta_0}^1 K(\eta; \ell) d\eta = \frac{S^2}{2S_- S_+} \int_{\eta_0}^1 K(\eta; \ell) d\eta \\ &= \frac{2}{1 - [\mathcal{A}(\ell, \eta_0)/\mathcal{A}(\ell, 1)]^2} \frac{1 - \sqrt{\eta_0^2 + \ell^2(1 - \eta_0^2)}}{1 - \ell^2}. \end{aligned} \quad (\text{S18})$$

While $\mathcal{U}/\mathcal{U}^*$ is not defined for passive particles $\eta_0 = \pm 1$, the limit of active particle with very small source or sink surface $\eta_0 \rightarrow \pm 1$ is well-defined:

$$\lim_{\eta_0 \rightarrow 1} \frac{\mathcal{U}}{\mathcal{U}^*} = \frac{1}{2} + \ell \frac{\sin^{-1} \sqrt{1 - \ell^2}}{2\sqrt{1 - \ell^2}} \stackrel{\ell \gg 1}{\simeq} \frac{1}{2} + \frac{1}{2} (\sin^{-1} 1) \ell. \quad (\text{S19})$$

The limit $\eta_0 \rightarrow -1$ is the same. For fixed aspect ratio ℓ , the (unscaled) speed is asymptotically ($\eta_0 \rightarrow 1$) given by multiplying the above limit by $\mathcal{U}^* \propto \|\Gamma\|/S$.

Similarly for source/inert configuration with active surface $\{\eta \geq \eta_0\}$ of area S_+ over which there is a uniform flux density $\|\Gamma\|/S_+$, we obtain

$$\begin{aligned} \text{source/inert: } \frac{\mathcal{U}}{\mathcal{U}^*} &= \frac{S}{\|\Gamma\|} \int_{-1}^1 K(\eta; \ell) \Gamma(\eta) d\eta = \frac{S}{\|\Gamma\|} \int_{\eta_0}^1 K(\eta; \ell) \frac{\|\Gamma\|}{S_+} d\eta = \frac{S}{S_+} \int_{\eta_0}^1 K(\eta; \ell) d\eta \\ &= \frac{2}{1 - \mathcal{A}(\ell, \eta_0)/\mathcal{A}(\ell, 1)} \frac{1 - \sqrt{\eta_0^2 + \ell^2(1 - \eta_0^2)}}{1 - \ell^2}. \end{aligned} \quad (\text{S20})$$

The limit of this scaled speed for a source/inert particle as $\eta_0 \rightarrow 1$ is twice the limit (S19) for the source/sink particle, but the limit as $\eta_0 \rightarrow -1$ is zero.

3. SELF-DIFFUSIOPHORESIS

In this section, we solve Popescu *et al.*'s model [5] of the bipartite source/inert self-diffusiophoresis, which has uniform flux α_+ on the region $\{-1 \leq \eta \leq \eta_0\}$ and zero flux elsewhere. Our notations are converted to those of [5] by the equivalences $\mu_{ph} \equiv -b$, $\mathcal{U} \equiv V$, $\alpha_+ \equiv \nu_B \sigma$, $\mathcal{D} \equiv D$. From Eqs. (S1) and (S13) we obtain the speed of this model as

$$V = \frac{(-\mu_{ph})\alpha_+}{2\mathcal{D}} \int_{-1}^{\eta_0} \frac{\eta}{\sqrt{\eta^2 + \ell^2(1 - \eta^2)}} d\eta = \frac{b\nu_B\sigma}{2D} \left[\frac{1 - \sqrt{\eta_0^2 + \ell^2(1 - \eta_0^2)}}{\ell^2 - 1} \right] = \frac{V_0}{2} \left[\frac{1 - \sqrt{\eta_0^2 + \ell^2(1 - \eta_0^2)}}{\ell^2 - 1} \right], \quad (\text{S21})$$

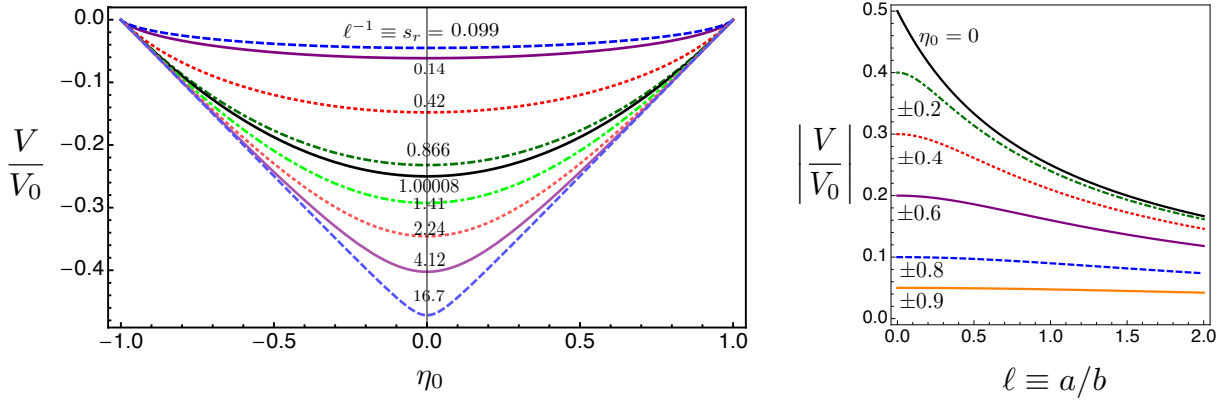


FIG. S1. Left: plot of Eq. (S21) corresponding to $s_r \equiv \ell^{-1}$ values in Fig. (4) of [5]. The speed is an even function of η_0 . Right: plot of Eq. (S21) as a function of aspect ratio for various values of η_0 . The speed is monotonically decreasing with increase in aspect ratio.

where $V_0 = b\nu_B\sigma/D$. This covers both the prolate and oblate cases which are given in series expansion form in Eqs. (32) and (34), respectively, of Ref. [5]. Limiting behaviors are extracted from this as (the spherical case, $\ell = 1$, is exact)

$$V \simeq \begin{cases} -(V_0/2)(1 - |\eta_0|), & \ell \rightarrow 0^+, \\ -(V_0/4)(1 - \eta_0^2), & \ell = 1, \\ -(V_0/2)\ell^{-1}\sqrt{1 - \eta_0^2}, & \ell \gg 1. \end{cases} \quad (\text{S22})$$

Equation (S21) and its limiting cases are all even in η_0 , and for a given aspect ratio ℓ the maximum speed $|V|_{\max}$ always belongs to antisymmetric ($\eta_0 = 0$) configuration. Also, for each value of η_0 , the maximum speed is for extreme discotic case $\ell \rightarrow 0^+$ and speed $|V|$ decreases monotonically with increase in aspect ratio ℓ as shown in Fig. S1.

References

- [5] M. N. Popescu, S. Dietrich, M. Tasinkevych, and J. Ralston, *Eur. Phys. J. E* **31**, 351 (2010).
- [7] A. Nourhani, V. H. Crespi, and P. E. Lammert, *Phys. Rev. E* **91**, 062303 (2015).
- [19] M. C. Fair and J. L. Anderson, *Journal Of Colloid And Interface Science* **127**, 388 (1989).